Acta Biomaterialia 151 (2022) 183–196

Contents lists available at ScienceDirect

Acta Biomaterialia

journal homepage: www.elsevier.com/locate/actbio

Full length article

Amniotic Membrane Enhances the Characteristics and Function of Stem Cell-Derived Retinal Pigment Epithelium Sheets by Inhibiting the Epithelial–Mesenchymal Transition

Suai Zhang[1], Ke Ye[1], Guanjie Gao, Xiaojing Song, Ping Xu, Jingrong Zeng, Bingbing Xie, Dandan Zheng, Liwen He*, Jianping Ji*, Xiufeng Zhong*

State Key Laboratory of Ophthalmology, Zhongshan Ophthalmic Center, Sun Yat-sen University, Guangdong Provincial Key Laboratory of Ophthalmology and Visual Science, Guangzhou, China

ARTICLE INFO

Article history:
Received 7 March 2022
Revised 22 July 2022
Accepted 29 July 2022
Available online 3 August 2022

Keywords:
Retinal pigment epithelial cells
Human amniotic membrane
Tissue engineering
Stem cell
Cell therapy

ABSTRACT

Human pluripotent stem cell-derived retinal pigment epithelium (iRPE) is an attractive cell source for disease modeling and cell replacement therapy of retinal disorders with RPE defects. However, there are still challenges to develop appropriate culture conditions close to *in vivo* microenvironment to generate iRPE sheets, which mimic more faithfully the characteristics and functions of the human RPE cells. Here, we developed a simple, novel platform to construct authentic iRPE sheets using human amniotic membrane (hAM) as a natural scaffold. The decellularized hAM (dAM) provided a Bruch's membrane (BM)-like bioscaffold, supported the iRPE growth and enhanced the epithelial features, polarity distribution and functional features of iRPE cells. Importantly, RNA-seq analysis was performed to compare the transcriptomes of iRPE cells cultured on different substrates, which revealed the potential mechanism that dAM supported and promoted iRPE growth was the inhibition of epithelial-mesenchymal transition (EMT). The tissue-engineered iRPE sheets survived and kept monolayer when transplanted into the subretinal space of rabbits. All together, our results indicate that the dAM imitating the natural BM allows for engineering authentic human RPE sheets, which will provide valuable biomaterials for disease modeling, drug screening and cell replacement therapy of retinal degenerative diseases.

Statement of significance

Engineered RPE sheets have a great advantage over RPE cell suspension for transplantation as they support RPE growth in an intact monolayer which RPE functions are dependent on. The substrates for RPE culture play a critical role to maintain the physiological functions of the RPE in stem cell therapies for patients with retinal degeneration. In this study, we constructed engineered iRPE sheets on the decellularized human amniotic membrane scaffolds, which contributed to enhancing epithelial features, polarity distribution and functional features of iRPE. dAM exhibited the ability of anti-epithelial mesenchymal transition to support iRPE growth. Furthermore, the results of transplantation *in vivo* demonstrated the feasibility of iRPE sheets in retina regenerative therapy. Engineering RPE sheets on dAM is a promising strategy to facilitate the development of iRPE replacement therapy and retinal disease modeling.

1. Introduction

Retinal pigment epithelium (RPE) is a monolayer of pigmented cells adjacent to the neuroretina. The RPE lies on Bruch's membrane (BM) and supports the survival and function of neuroretina via many functions, including 1) transport of water, nutrients and ions; 2) stray light absorption; 3) re-isomerization of all-*trans* retinol during the visual cycle; 4) phagocytosis of photoreceptor

* Corresponding authors.
E-mail addresses: heliwen@mail.sysu.edu.cn (L. He), jpji1974@126.com (J. Ji), zhongxf7@mail.sysu.edu.cn (X. Zhong).
[1] These authors contributed equally to this work and should be considered as co-first authors

https://doi.org/10.1016/j.actbio.2022.07.064

outer segments (POS); 5) polarized secretion of essential factors and 6) maintaining of the blood-retina barrier [1]. Therefore, RPE dysfunction has been involved in a wide range of retinal degenerative diseases such as age-related macular degeneration (AMD) and retinitis pigmentosa (RP), which are two major causes of irreversible blindness without effective treatment worldwide.

With the advances in stem cell research, the successful generation of human pluripotent stem cell-derived RPE (iRPE) facilitates not only the development of regenerative therapy but also the elucidation of mechanisms underlying RPE-related diseases by modeling pathogenesis [2,3]. Especially in regenerative therapy, transplantation of iRPE sheets or cell suspension for AMD patients is proven to be safe and potentially effective [4–9]. However, the outcome of RPE suspension transplantation in AMD patients is not consistent because suspended RPE cells hardly self-organize into a polarized monolayer in subretinal space, and thus affect their long-term survival. Compared to the injection of iRPE suspension, the transplantation of tissue-engineered iRPE sheets may improve therapeutic outcomes because the survival of transplanted cells is better [10]. The next stage is development of clinically compatible iRPE sheets with full functions, which is still challenging.

One of the major issues in the field of RPE sheet construction is the development of a BM substitute for the growth and graft of iRPE cells. The native BM is approximate 3 μm in thickness and consists of five layers: the basement membrane of the RPE, the inner collagenous layer (ICL), the elastin layer (EL), the outer collagenous layer (OCL) and the basement membrane of the choriocapillaris. It contains complex extracellular matrix (ECM) components such as laminin, fibronectin, collagens, elastin, glycosaminoglycans hyaluronic acid and dermatan sulphate [11]. Importantly, BM plays a key role in RPE biological processes, which is necessary to maintain the normal function of neural retina. For example, the healthy BM regulates diffusion of biomolecules between choroid and RPE as a semi-permeable filter, and provides physical support for cell adhesion, migration and differentiation of RPE cells [11]. In contrast, the pathogenic changes of BM affect the cell behavior and functions of RPE, causing various retinal disorders. The accumulation of lipid and advanced glycation end products has been identified in the aged BM, which is considered as one of the causative factors of AMD [12]. Therefore, the development of a biocompatible BM-like scaffold for iRPE cultivation will contribute to not only the generation of full functional iRPE sheets for cell replacement therapy but also to the modeling and drug discovery of retina diseases.

In the past decade, several synthetic or natural BM-like scaffolds have been explored in engineering RPE sheets with advantages and disadvantages. The biodegradable synthetic scaffolds including polyester, poly (lactic acid) (PLA), poly (lactic-co-glycolic acid) (PLGA), and poly (ε-caprolactone) (PCL) have been developed for supporting RPE delivery, which are considered as biocompatible [13–15] (ClinicalTrials.gov NCT01691261, NCT03102138, NCT02590692). However, safety is a concern because their degradation products can cause widespread retinal degeneration after subretinal transplantation [16]. To solve these issues, natural BM-like scaffolds, such as the Descemet's membrane or the lens capsule, have been tried to support RPE cell growth as monolayer structures [17,18]. Nevertheless, the limited sources restrict their broad applications. As another natural scaffold, the human amniotic membrane (hAM), which is readily available and inexpensive, has been broadly used in ocular surface reconstruction or wound dressing [19]. Although hAM possesses many structural and functional features close to the native BM such as enrichment of ECM, high elasticity, permeability and stability [11], there are only a few reports on its application in retinal reconstruction [20,21]. One of the possible reasons may be due to the lack of technical skills which can simply fix the hAM in the right orientation for cell growth and graft. In addition, the underlying effect of hAM on RPE cell growth *in vitro and in vivo* is largely unclear.

This study aimed to generate an authentic iRPE sheet on hAM for clinical and research applications. We developed a decellularized hAM (dAM) scaffold culture chamber by simple fixation with two clamps to support the long-term culture of iRPE cells. The bioengineered dAM-iRPE sheets were thoroughly evaluated in molecular, morphological and functional levels. dAM affected the cellular responses of iRPE cells, which contributed to enhancing the gene expression, morphological and functional features when compared to iRPE cultured on plastic culture dish or transwell. The mechanism of iRPE on dAM with an authentic characteristic was dAM inhibited the epithelial-mesenchymal transition (EMT) process. We further transplanted the tissue-engineered iRPE sheets into the subretinal space of rabbits and preliminarily demonstrated the feasibility of iRPE sheets in retina regenerative therapy. The construction of dAM for iRPE cultivation, combined with the thorough evaluation of the tissue-engineered iRPE sheets, has the potential to the application for RPE replacement therapy and RPE disease modeling.

2. Materials and methods

2.1. De-epithelialization of human amniotic membrane

The study followed the tenets of the Declaration of Helsinki. The cryopreserved hAM was provided by the Eye Bank of Guangdong Province, China. It was thawed at room temperature and decellularized according to the reported protocol with slight modification [22]. Briefly, the hAM was placed carefully with the epithelial surface facing upward in a 100 mm petri dish, rinsed in phosphate buffered saline (PBS) twice, and then treated with 0.1% trypsin/0.4 mM EDTA (Gibco, Grand Island, NY, USA) for 12–15 min at 37 °C. After the incubation, the dissociated epithelial layer of the hAM was rinsed in PBS twice and observed under an inverted microscope (Zeiss, Jena, Germany) to ensure the removal of entire epithelial layer. The transparency of hAM and dAM was visually evaluated with letter "A" underlying the membranes [23]. Nuclear staining with DAPI was performed to further confirm the completeness of de-epithelization.

2.2. Manual setup of dAM scaffold chambers for iRPE cultivation

To lower the cost and increase the accessibility, a dAM scaffold chamber was developed by manual fixation with a tissue carrier (Minucells and Minutissue, Bad Abbach, Germany). The tissue carrier consisted of two rings: a black holding ring and a smaller white ring. The outer diameter of this carrier was 13 mm and the inner diameter 9 mm (Fig. S1A). Firstly, the dAM was placed over the black ring with the basement membrane facing up. Secondly, the white ring was downward inserted into the black holding ring to fix the dAM and keep it in the appropriate tension without foldings and holes. Thirdly, the excessive dAM outside the cell carrier was cut. Finally, the established dAM chambers compatible with various types of culture vessels were transferred into 24-well culture plates containing PBS. Sterility testing was performed before use.

2.3. Cell strain and culture of RPE cell sheets

iRPE cells were induced from BC1 and BC1-GFP hiPSCs, enriched, expanded and cryopreserved in our laboratory according to the previous report [24]. To generate iRPE sheets, the frozen iRPE cells were revived and cultured on Matrigel-coated 6-well culture plates. When reached confluence, the iRPE cells were dissociated and seeded on different substrates: dAM scaffold cham-

ber, transwell membrane coated with Matrigel (TM) and tissue culture plate coated with Matrigel (TCP) in the same density of 1×10^5 cells/cm^2. The cells were cultured in medium containing 50% DMEM/F12 (Gibco), 35% DMEM basic (Gibco), 10% FBS (Gibco), 2% B27 supplement (Gibco), 1% NEAA (Gibco), 1% GlutaMax (Gibco), 0.1% Taurine (Sigma-Aldrich, St. Louis, MO, USA) and 1% penicillin-streptomycin (Gibco). After cells grew into confluence in 10 days, the culture medium was switched into RPE maturation medium consisting of 60% DMEM/F12, 37% DMEM basic, 2% B27 supplement, and 1% penicillin-streptomycin. Cells were observed and imaged with inverted microscope (Zeiss).

2.4. Atomic force microscopy (AFM)

AFM was used to detect the stiffness of dAM, TM and TCP. The measurements were performed in liquid (PBS on the apical side of the membrane). For the measurement, substrate samples were bonded on a coverslip. All the experiments were performed by an atomic force microscope (Dimension FastScan, Bruker, Germany). Force−volume images were acquired within a square of 20 μm $\times$ 20 μm at the center of the membrane. An AFM tip with an adhered 5 μm radius polystyrene sphere and silicon nitride cantilever applied to obtain the force-separation curves. A minimum of 64 points were measured per membrane. DMT modulus was selected to measure the parameter of Young's modulus, which refers to the relationship between stress and strain in a material. A stiffer material exhibits a higher Young's modulus.

2.5. Immunohistochemistry

Immunostaining was performed as described previously [24,25]. For cryosections of iRPE, hAM and dAM, samples were fixed with 4% paraformaldehyde (PFA) for 15 min at room temperature. After dehydration in gradient sucrose solution and embedding in OCT compound (Sakura Finetek Japan, Tokyo, Japan), tissues were sectioned in 16 μm thickness. For iRPE flatmounts, iRPE sheets were washed and fixed in 4% PFA for 15 min at room temperature. After blocking and permeabilization, the cryosections or flatmounts were incubated with the following primary antibodies overnight in 4°C: mouse anti-ZO-1 (1:400, Thermo Fisher Scientific, Waltham, MA, USA); mouse anti-BEST1 (1:500, Abcam, Cambridge, UK); rabbit anti-OTX2 (1:500, Abcam); rabbit anti-PMEL17 (1:500, Abcam); mouse anti-EZRIN (1:100, Abcam); mouse anti-CRALBP (1:500, Abcam); mouse anti-Na/K ATPase (1:200, Abcam); mouse anti-α-SMA (1:500, Abcam); rabbit anti-collagen IV (1:200, American Research Products), mouse anti-laminin (1:100, Boster, Wuhan, China). Following PBS washing, samples were incubated with appropriate secondary antibody (1:500, Donkey anti-Mouse, Alexa Fluor 555, Invitrogen, Carlsbad, USA; Donkey anti-Rabbit, Alexa Fluor 555, Invitrogen; Donkey anti-Rabbit, Alexa Fluor 488, Invitrogen; Donkey anti-Rabbit, Alexa Fluor 647, Invitrogen) for 1 hour at room temperature. For labeling of F-actin, fixed cells were treated with TRITC Phalloidin (Solarbio, Beijing, China) for 30 min after blocking and permeabilization. Nuclear staining was performed with DAPI. Images were acquired using either Zeiss LSM 880 confocal microscope (Carl Zeiss) or ZEISS Axio observer 7 microscope (Carl Zeiss).

2.6. Hematoxylin-eosin (H&E) staining

For H&E staining of hAM and dAM, 6 μm thick of cryosections were washed and stained with hematoxylin (Biosharp, Hefei, China) and eosin (Beyotime Biotechnology, Shanghai, China) as described previously [26]. Images were acquired using ZEISS Axio observer 7 microscope. The thickness of hAM and dAM was measured by Fiji software (National Institutes of Health, Bethesda, USA).

2.7. RPE flatmount image segmentation and morphometric analysis

For morphometric analysis of individual RPE cells in each flatmount image, we segmented RPE cells from images of ZO-1 staining which labeled the cell borders. Following the process including making binary, despeckling and removing abnormal cells in a semi-automatic way, an individual cell was recognized in Fiji software. Using the binarized images, the following morphometric features were measured: cell area, form factor and number of cell neighbors. Cell area represented the size of each iRPE cell. Form factor reflected the relationship of perimeter to area according to the definition $4\pi \times \text{area}/\text{perimeter}^2$, which has been used to measure the deviation of a cell from the shape of perfect hexagon [27]. The form factor value for the perfect equilateral hexagon is 0.84. When the form factor of a cell is close to 0.84, this cell's shape is closed to that of native RPE cells. Analysis of cell neighbors was used to count the number of contacting neighbor cells for calculating the ratio of hexagonal cells. If there were more hexagonal cells in an iRPE sheet, this iRPE sheet was considered to have the better quality. Over 200 cells were randomly picked from three different samples in each group to conduct this analysis.

2.8. Analysis of pigmentation

The appearance of the iRPE pigmentation on each substrate was recorded by inverted microscope . The degree of pigmentation was analyzed 4 weeks after cultivation by randomly capturing 20 $\times$ bright field images with ZEISS Axio observer 7 microscope. The quantification of pigmented area was performed by Fiji software. Briefly, bright field images were binarized to 8-bit images to reflect the pigmented area (high intensity) and unpigmented area (low intensity). The images threshold was determined to measure percentage of the high intensity area. Three to ten images from each group were used to analyze.

2.9. Phagocytosis Assay

The phagocytosis assay was performed as previously described [24]. Photoreceptor outer segments (POS) were generated from porcine eyes in a dark room and labeled with CM-Dil (C7001; Invitrogen) following manufacturer instructions. iRPE on different substrates at 6 weeks were treated with the CM-Dil labeled POS at 37 °C or 4 °C (negative control) for 24 h. Afterward, all the samples were washed with PBS thoroughly, fixed with 4% PFA and stained with DAPI. Images were acquired with a ZEISS Axio observer 7 microscope. For quantitative analysis, the number of cells and POS were counted using Fiji software from five random fields of view (40 $\times$) in each group. In the functional comparison of iRPE cells in different substrates, the amount of POS was normalized by the number of cells in each image.

2.10. ELISA of VEGF secretion

Before the experiments, iRPE cells were washed with PBS twice then cultured in 500 µL DMEM-basic for 24 h. The culture supernatants were collected and centrifuged at 300 $\times$ g for 5 min before quantification of VEGF concentration. The measurement was performed by three different samples using the human VEGF Quantikine ELISA kit (QuantiCyto, Wuhan, China) according to manufacturer instructions. In the functional comparison of iRPE cells in the different substrate, the concentration of VEGF was normalized by the culture area.

2.11. Electron microscopic analysis: scanning electron microscopy (SEM) and transmission electron microscope (TEM)

iRPE sheets on dAM were fixed in the modified Karnovsky's solution (2.5% glutaraldehyde/2% PFA) at 4°C before processing, which was performed in Electron Microscopy Core Facility of Sun Yat-sen College of Medical Science, Sun Yat-sen University (Guangzhou, China). For SEM analysis, hAM, dAM and iRPE sheets were dehydrated in a graded series of ethanol/water, transferred into 100% acetone for 15–20 min, 100% isoamyl acetate for 15–30 min. Samples were dried using the Leica EM CPD 300, and sputter-coated with gold using the Coater Ion sputter EIKO IB-5. Finally, samples were analyzed with the SEM (FEI Quanta 200) at 5 kV acceleration voltage using the lower secondary electron detector.

For TEM analysis, iRPE sheets on dAM were dehydrated by passing through a graded series of ethanol solutions, and embedded in epoxy resin. Then samples were cut into ultrathin sections with an ultra-microtome, stained with 1% uranyl acetate and lead citrate, and then imaged with a transmission electron microscope (FEI Europe, Eindhoven, Netherlands).

2.12. RNA-seq and data analysis

iRPE cells (about 1×10^6 cells per experiment, 2 experiments) from different groups were collected in Trizol reagent (Invitrogen) and stored in a −80 °C freezer until submitted to Gene Denovo Biotechnology Co (Guangzhou, China) for RNA extraction, library preparation, sequencing and data analyses. Total RNA was extracted according to the manufacturer's instructions. RNA quality and quantity were assessed using the Agilent 2100 bioanalyzer (Agilent Technologies). mRNA libraries were then generated and RNA-seq was performed by Illumina Novaseq6000.

Raw data were processed using the fastp tool (version 0.18.0). Reads containing poly-Ns, duplicate sequences, and low-quality sequences were removed to obtain high-quality clean reads. The remaining clean reads were further used in assembly and gene abundance calculation. Gene expression levels were quantified by software RSEM [28]. The fragment per kilobase of transcript per million mapped reads (FPKM) value was calculated to quantify the expression levels of each gene. Correlation analysis was performed by R. correlation of two parallel experiments. Principal component analysis (PCA) was performed with R package g models (http://www.r-project.org/). Differential expression analysis was performed by DESeq2 R package (1.18.0) between two different groups and by edgeR (Robinson et al., 2010) between two samples. The genes/transcripts with the parameter of false discovery rate (FDR) below 0.05 and absolute fold change ≥2 were considered differentially expressed genes (DEGs). Then the DEGs were subjected to Gene Ontology (GO) and Kyoto Encyclopedia of Genes and Genomes (KEGG) pathway enrichment analysis. The GO terms or pathways with a Qvalue ≤ 0.05 were defined as significantly enriched. Gene set enrichment analysis (GSEA) was further performed using software GSEA and MSigDB [29]. Enrichment scores and p value were calculated as default parameters, and $p<0.05$ was considered statistically significant.

2.13. Subretinal transplantation and in vivo imaging

The *in vivo* experiment was approved by the Animal Experimental Ethics Committee of the Zhongshan Ophthalmic Center, Sun Yat-sen University. All experiments were conducted in accordance with the Association Research in Vision and Ophthalmology (ARVO) Statement for the Use of Animals in Ophthalmic and Vision Research. New Zealand white albino rabbits aged 6 months, weighing between 3.5 to 4.0 kg were used in this study. Rabbits were treated daily with cyclosporine A 3 days before the experiment. Before surgery, rabbits were anesthetized with intramuscular injection of pentobarbital sodium (1 mg/kg) and Xylazine hydrochloride (1 mg/kg), and pupils were dilated. After the scleral incision was made using 23 G trocar (Alcon, Fort Worth, TX, USA), subretinal blebs were created by injection of PBS under a surgical microscope (Leica, Wetzlar, Germany). 2 to 3 mm^2 of dAM-iRPE sheets were grafted into the subretinal space by a microforceps and a microneedle. Multi-color fundus images, BluePeak autofluorescence (BAF) and spectral-domain optical coherence tomography (SD-OCT) were performed to evaluate the grafts *in vivo* with a SPECTRALIS HRA+OCT instrument (Heidelberg Engineering, Heidelberg, Germany) 7 days after surgery. After observation, rabbits' eyes were enucleated and fixed with 4% PFA for cryosection and immunostaining.

2.14. Statistical analysis

Values were expressed as mean ± standard deviation (SD). Statistical analysis was performed with GraphPad Prism version 9.0. The statistical significance of difference was determined by unpaired t-test for two-group comparisons or ANOVA followed by Dunnett's test for three-group comparisons. $P < 0.05$ was considered statistically significant. For statistical analysis of RNA-seq, see '2.10. RNA-seq and data analysis' for more details.

3. Results

3.1. Evaluation of dAM scaffolds for iRPE sheet generation

To provide the dAM bioscaffold for culturing the iRPE cells, the epithelial layer of hAM was removed before iRPE seeding. After thawing, hAM fixed on a nitrocellulose membrane was treated by trypsin/EDTA (Fig. S1B). The cell debris was observed after treatment (Fig. S1C). Compared to the hAM, the dAM was more transparent as the letter "A" beneath the membrane was clearer (Fig. 1A). Bright-field microscopic images and DAPI labeling confirmed that the dAM was lack of epithelial cells (Fig. 1B). H&E staining of cryosections of hAM and dAM revealed that the thickness of dAM was thinner than hAM after trypsinization because of the removal of epithelial cells (Fig. 1C, D). The ultrastructure analysis by SEM confirmed that only a dense fibroid structure was identified in dAM surface, whereas the hexagonal epithelial cells were observed in hAM (Fig. 1E). To further analyze whether the components changed in dAM, immunostaining for two key components of ECM, collagen IV and laminin, was performed. Both of them were not remarkably changed (Fig. 1F). Because they are also two major ECM components in BM as well [11], these results suggested that trypsin treatment could efficiently and gently remove the epithelial layer of hAM without the influence on ECM, producing an important natural substrate of dAM to support RPE cell growth.

Following the de-epithelialization, the dAM was manually fixed with two holding rings to establish a culture chamber fitting to various types of culture vessels (Fig. S1D). In this study, the dAM-based cultivation chamber was used for the culture of iRPE cells unless otherwise stated (Fig. S1E).

3.2. Characterization of iRPE sheets on dAM scaffold

The preparation of iRPE sheets on dAM scaffold was schematically illustrated in Fig. 2A. When growing on dAM with an initial density of 1×10^5 cells/cm^2, the iRPE cells quickly became confluent, and gradually presented homogeneous, polygonal morphology within six weeks after culture (Fig. 2B). Melanin was observed in the apical side of iRPE sheets (Fig. 2C). Immunofluorescence staining showed that integrin $\beta 1$ and collagen IV located in the basal

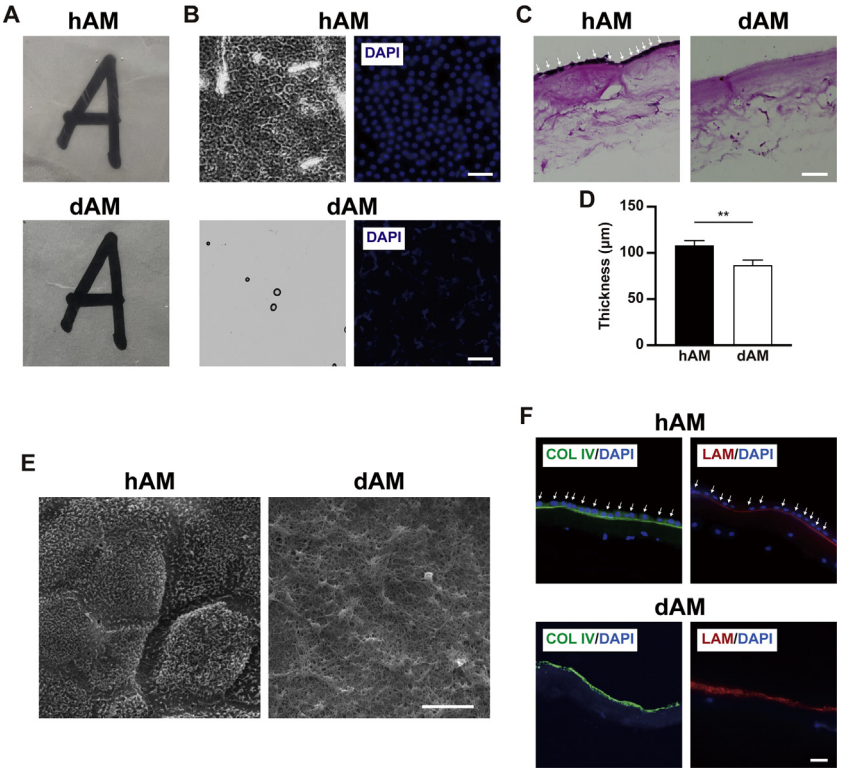

Fig. 1. Characterization of dAM scaffold for iRPE cultivation. (A) Comparison of macroscopic photographic images of hAM and dAM in moist form. dAM showed higher transparency. (B) Representative phase-contrast images and DAPI staining of hAM and dAM. No epithelial cells and a small amount of DNA were detected in dAM. Scale bar = 50 μm. (C) Representative H&E staining of vertical section of hAM and dAM. No epithelial cells were detected in dAM. Arrows indicated epithelial cells in hAM. Scale bar = 50 μm. (D) Quantification of thickness of hAM and dAM. Values were expressed as mean ± SD ($n = 4$). ** $P < 0.01$, compared to hAM. (E) Representative SEM images of epithelial side of hAM and dAM. Scale bar = 5 μm. (F) Immunostaining for collagen IV and laminin of hAM and dAM. Scale bar = 20 μm. Arrows indicated the signal of DAPI.

side of dAM-iRPE sheets, while ZO-1 located in the apical side, indicating that iRPE sheets were polarized (Fig. 2D, E). In addition, other RPE-specific markers including BEST1, OTX2, CRALBP, PMEL, EZRIN and Na/K ATPase were also highly expressed and located in the correct side of dAM-iRPE sheets, confirming they grew into matured iRPE sheets after cultured on dAM for 6 weeks (Fig. 2F). The ultrastructures of RPE cells grown on dAM were further evaluated. SEM and TEM images showed that they had a well-organized polygonal shape with long microvilli on their apical side, basal infoldings, melanin granules and tight junction (Fig. 2 G-K), which are characteristics of human native RPE. Taken together, our results indicated that the dAM supported the growth of iRPE cells into matured RPE sheets with well-organized epithelial features.

3.3. Enhancement of morphological and functional features of iRPE on dAM scaffold

RPE cells (including primary RPE and iRPE) have been commonly cultured on tissue culture plates or semipermeable transwells. Compared to these two culture vessels, whether dAM has the potential to further enhance the characteristics of RPE is still unknown. To achieve this, iRPE cells cultured on three different surfaces of dAM, TM and TCP were further compared in cellular processes after adhesion, morphometric and functional features of mature epithelial cells.

After cell attachment, the F-actin organization changes in response to the features of substrate [30]. When seeded on three different substrates for 1 day, iRPE cells presented different F-actin distribution: the circumferential actin belt was remarkably observed in iRPE cells on dAM, whereas iRPE cells on TM or TCP exhibited more radial stress fibers than those on dAM (Fig. 3A, B). Because stiffness is one of the important factors that affect cell reaction after seeding, we measured Young's modulus of three different scaffolds using AFM. TM and TCP had higher values of Young's modulus than dAM (Table 1).

We further analyzed the morphological features of iRPE cells cultured on different substrates. In the first 7 days after seeding, some cells on TM or TCP represented fusiform morphology, which was a typical phenotype of RPE cells in a dedifferentiation process. These spindle-like cells were still observed even at 4 weeks after culture (Fig. 3C). In contrast, iRPE on dAM gained a cobblestone-like morphology in one week and became highly homogeneous in 4 weeks after culture (Fig. 3C). To compare the morphometric features, ZO-1 labeled images of iRPE cells after 6 weeks' culture on three different substrates were applied to extract the morphometric information (Fig. 3D). Images were processed by Fiji software to obtain binary images. After cell recognition, the data of cell area, form factor and cell neighbors were extracted (Fig. S2A). Compared to iRPE cells growing on TM or TCP, iRPE cells on dAM had the smallest cell area (Fig. 3E, S2B). In addition, the form factor of iRPE cells on dAM, TM and TCP was 0.78 ± 0.11, 0.71 ± 0.13, 0.69 ± 0.14, respectively. Therefore, the former had the most similar value to that of the perfect hexagon among the three groups (Fig. 3F, S2C). When calculating the number of neighboring cells in each group, the ratio of hexagonal cells in iRPE cells on dAM (36% ± 4.0%) was significantly higher than those on TM (26% ± 6.4%) or TCP (28% ± 2.8%) (Fig. 3G). The morphometric features of iRPE cells on dAM were similar to those of human native RPE cells *in vivo* [27].

To assess the advantage of dAM, we compared the cell pigmentation and the cellular function among the three groups. Pigmentation is one of the features commonly used to indicate the maturation of iRPE cells. The differences in the density of pigmentation

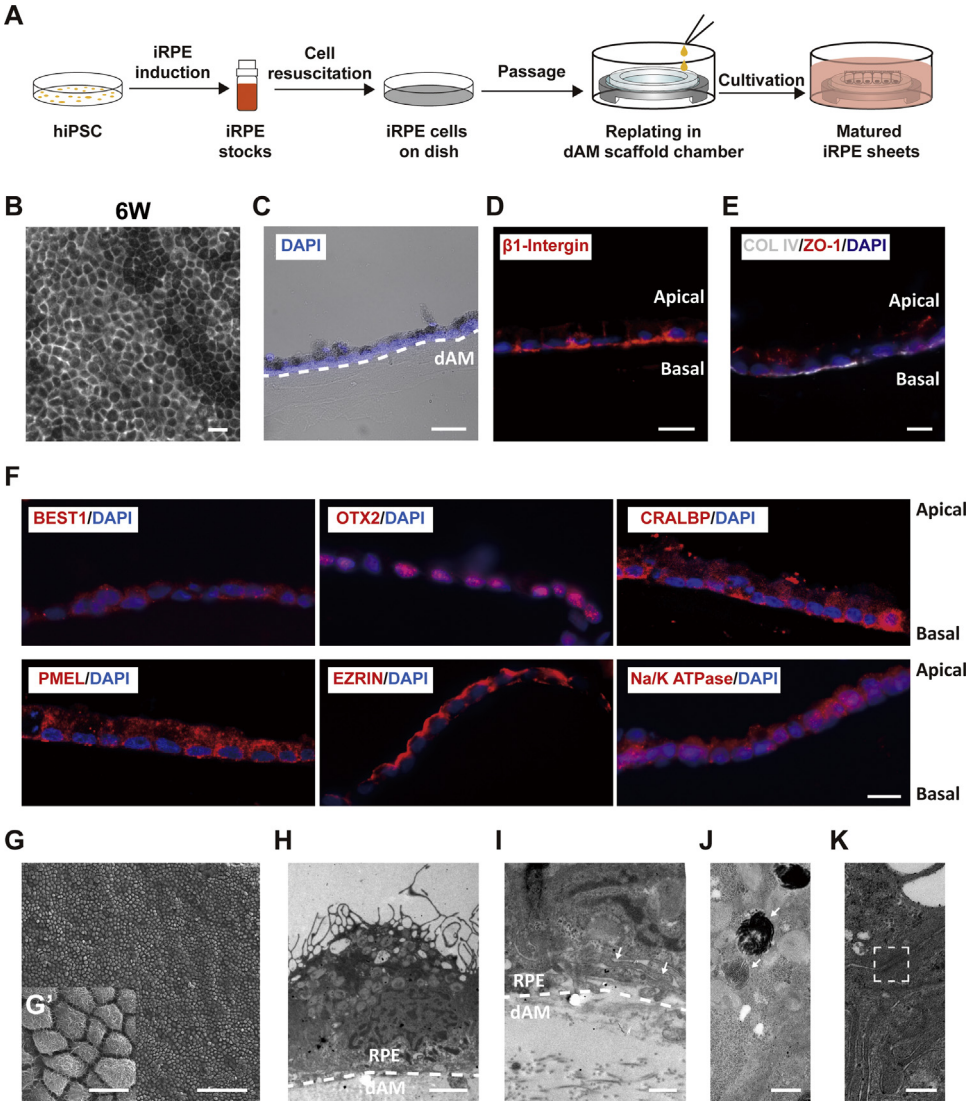

Fig. 2. Cultivation and characterization of iRPE cells on dAM scaffold. (A) Schematic illustration of cultivation of iRPE cells in dAM scaffold chambers. (B) Representative phase-contrast images of iRPE cells cultured in dAM chambers for 6 weeks (6W). Scale bar = 20 μm. (C) Representative microscopic image of a vertical section of dAM-iRPE sheets. Nuclei was labeled by DAPI. Scale bar = 20 μm. (D-F) Representative immunofluorescence images of dAM-iRPE for β1-integrin, collagen IV and ZO-1, BEST1, OTX2, CRALBP, PMEL, EZRIN and Na/K ATPase. Scale bar = 10 μm. (G, G') SEM images of iRPE on dAM at different magnification. Each iRPE cell showed similar morphology with long apical microvilli. Scale bars, 100 μm (G), 10 μm (G'). (H-K) Characterization of iRPE on dAM by TEM. After cultivation on dAM for 6 weeks, iRPE cells presented microvilli (H), basal infoldings (I), melanin granules (J) and tight junction (K). Scale bars, 2 μm (H), 500 nm (I, J), 200 nm (K). Arrows indicated the basal infoldings (I) and melanin granules (J). Dashed line showed the boundary of cell body and dAM (I).

Table 1
Young's modulus of dAM, TM and TCP using AFM.

	dAM	TM	TCP
Young's modulus (Compression)	1.22–5.50 KPa	211.40–659.78 KPa	70.72–175.93 MPa

were observed by microscopy. The pigmented cells were homogeneous on dAM, but distributed in clusters on the TM and TCP. In addition, over 29% of cells exhibited high degree of pigmentation, whereas those on TM and TCP had a lower production of pigmentation (Fig. 4A, B). In the comparison of cellular function, phagocytosis and cytokine secretion assays were performed with iRPE cells from three different groups. Phagocytosis of the outer segments shed from photoreceptors is one of the essential functions of the polarized RPE monolayer. After feeding POS to iRPE cells for 24 h, more POS were phagocyted in iRPE cells on dAM than on TM and TCP (Fig. 4C, D). Furthermore, iRPE cells on dAM also secreted a significantly higher amount of VEGF (Fig. 4E). Overall, our results demonstrated that dAM scaffold supported iRPE cells to grow into authentic human RPE, which exhibited better morphology and functionality.

3.4. Transcriptome analysis of iRPE cells on different substrates

To characterize and compare the transcriptome profiles of iRPE cells cultured on different scaffolds, we performed RNA-seq of iRPE cells cultured on dAM, TM and TCP. In both PCA and sample correlation analysis, iRPE cells from the same substrate were grouped together, indicating high reproducibility of biological replicates (Fig. 5A, B). Differential expression analysis showed that when compared with dAM, the number of DEGs that showed more than or equal to two-fold change in TCP or TM group was 1433 and

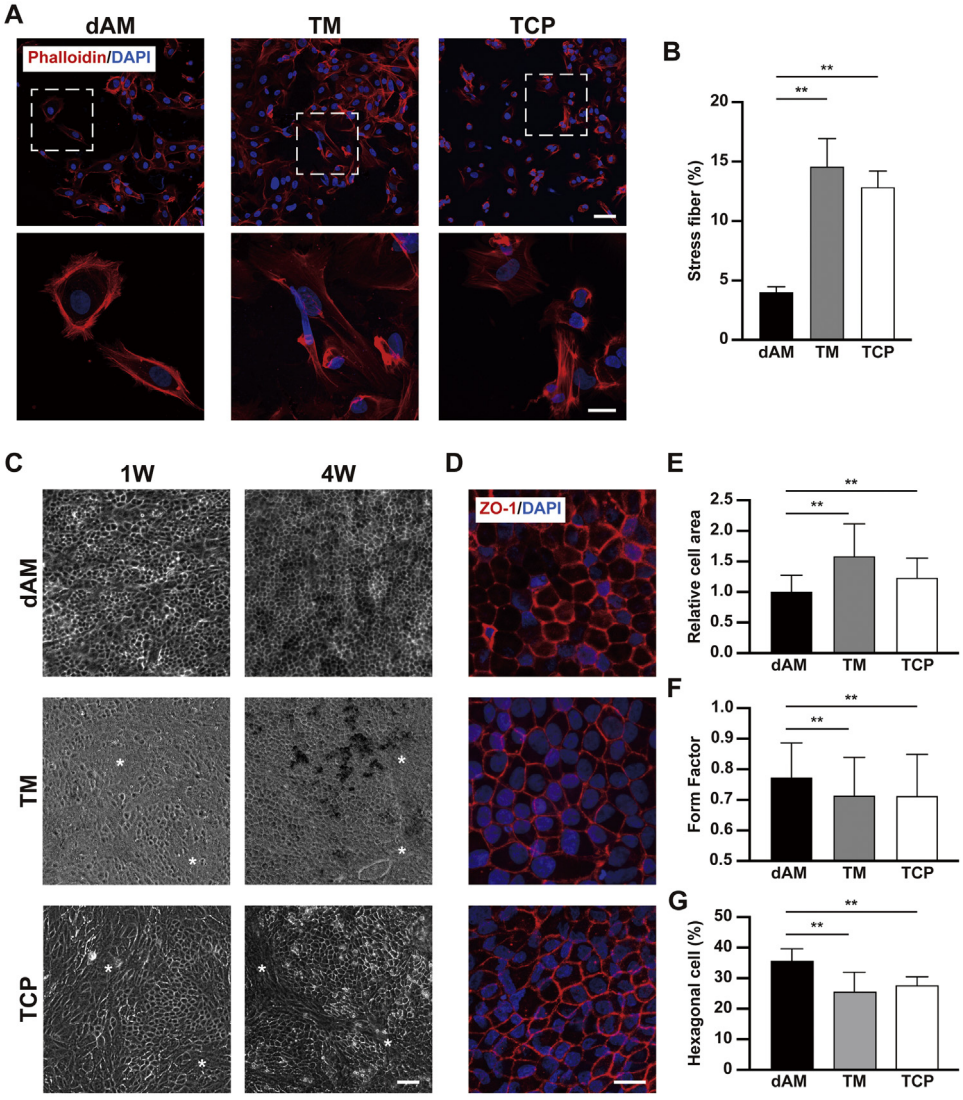

Fig. 3. Enhancement of morphological features in iRPE cells on dAM. (A) Representative phalloidin staining for F-actin in iRPE cells on dAM, TM and TCP after seeding for 1 day. Scale bar = 20 μm. (B) Quantification of percentage of cells with stress fiber among iRPE cells on different scaffolds. Values were expressed as mean ± SD (n = 3). ANOVA followed by Dunnett's test; ** P < 0.01, compared to dAM. (C) Representative phase-contrast images of iRPE cells on dAM, TM and TCP after seeding for 1W and 4W. Scale bar = 50 μm. Asterisk indicated the spindle-like cells. (D) Representative whole-mount immunofluorescence images of iRPE sheets on dAM, TM and TCP for ZO-1. Scale bar = 20 μm. (E) Quantification of cell area among iRPE cells on different scaffolds. Values were expressed as mean ± SD (n = 263 cells from 3 different samples). ** P < 0.01, compared to dAM. (F) Quantification of cell eccentricity of iRPE cells on different scaffolds. Values were expressed as mean ± SD (n = 303 cells from 3 different samples). ** P < 0.01, compared to dAM. (G) Analysis of percentage of hexagonal cells among iRPE on different scaffolds by quantification of cell neighbors. Values were expressed as mean ± SD (n = 11–14 images from 3 different samples). ** P < 0.01, compared to dAM.

1138, respectively. In contrast, compared with TCP, there were only 139 DEGs in TM group (Fig. 5C, S3). These results indicated that there were significant differences in the transcriptomes of iRPE cells between dAM and the other substrate groups.

Next, we compared the expression of the RPE-specific genes in iRPE cells cultured on different substrates. Compared to TM and TCP, melanin metabolism-related genes were up-regulated in dAM group (Fig. 5D). Especially the expression of *TYR, TTR, SLC24A5, PMEL* and *KIT* was significantly higher in iRPE sheets on dAM (Fig. 5E). In addition, the up-regulation of the expression of RPE functional genes was identified in dAM group (Fig. 5F), especially the genes associated with vitamin A metabolism (*RDH5, LRAT, RLBP1*), volume regulation (*BEST1*) and phagocytosis (*MERTK*) (Fig. 5G). Collectively, these transcriptomic findings further demonstrated that dAM could promote the functional maturation of iRPE, which was consistent with the results in the functional analysis described above (Fig. 4).

3.5. Highlight of the anti-EMT effect of dAM in iRPE cells cultivation

Finally, the mechanism that dAM promoted iRPE growth into authentic, cobblestone like human RPE was explored. Among three different surfaces, almost all of cells on dAM presented epithelial morphology, while part of the iRPE cells cultured on TM or TCP exhibited a fibroblast-like morphology (Fig. 3C). This fibroblast-like shape is a typical property of RPE cells under EMT process [36]. In addition, immunostaining for α-SMA, a mesenchymal marker to indicate EMT, showed that α-SMA positive cells were hardly seen in the iRPE cultured on dAM, but observed on TM and TCP (Fig. 6A, B), indicating the suppression of EMT in iRPE cells cultured on dAM when compared with the TM and TCP groups.

Moreover, with the RNA-seq data, 15 of the most significantly changed signaling pathways between iRPE cells cultured on dAM and TM or TCP were identified by KEGG analysis. Among them, focal adhesion, regulation of actin cytoskeleton and pathways in

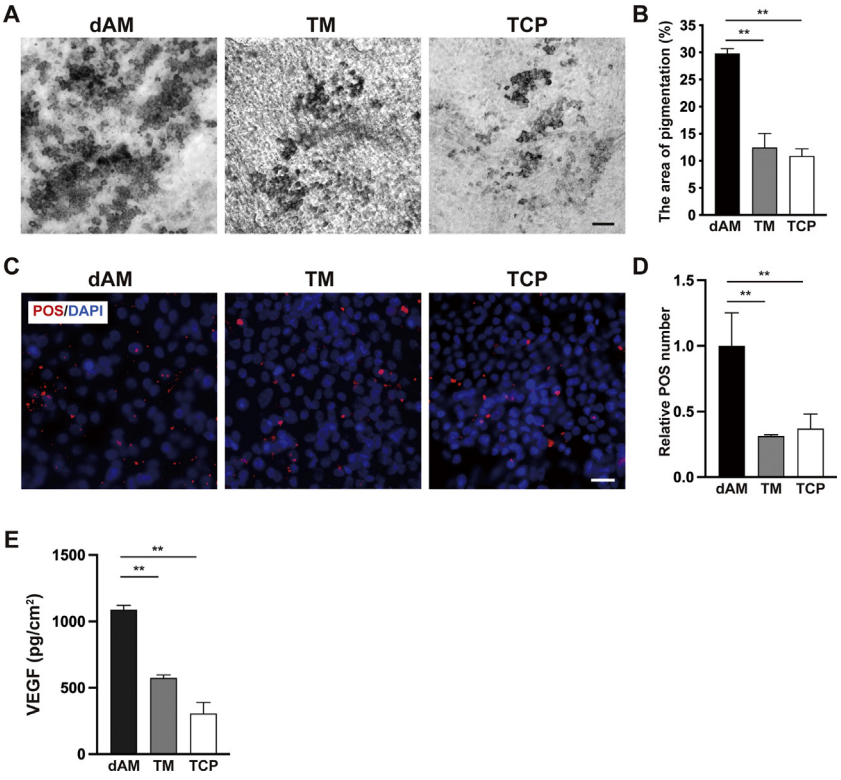

Fig. 4. Enhancement of pigmentation and cellular function in iRPE sheets on dAM. (A) Representative bright field images of iRPE cells on three different scaffolds at week 4. Scale bar = 50 μm. (B) Quantification of pigmentation area among iRPE cells on different scaffolds. Values were expressed as mean ± SD (n = 3). ** P < 0.01, compared with dAM. (C) Representative images of iRPE cells on different scaffolds 24 h after exposure of CM-Dil labeled POS (red). Nuclei were co-stained with DAPI (blue). Scale bar = 20 μm. (G) Quantification of the number of POS in iRPE cells on different scaffolds. Values were expressed as mean ± SD (n = 3 ~ 4). ** P < 0.01, compared to dAM. (H) Quantification of VEGF secreted by iRPE cells on different scaffolds using an ELISA assay. Values were expressed as mean ± SD (n = 3). ** P < 0.01, compared to dAM. (For interpretation of the references to colour in this figure legend, the reader is referred to the web version of this article.)

cancer were associated to EMT of RPE cells (Fig. S4A, B) [31]. Additionally, GSEA analysis notably indicated the inhibition effect of dAM on EMT (Fig. 6C, D) [29]. Differential expression analysis also showed that genes involved in promoting EMT process were down-regulated in iRPE cells on dAM, such as *SNAI2, VIM, CDH2, FGF2* and *TGFB1* (Fig. 6E, F), while genes inhibiting EMT progress were up-regulated, such as *BMP7, SFRP5, AXIN2* and *NOG* (Fig. 6E, F). Furthermore, when compared to dAM group, the known ECM genes such as *LAMA1, COL4A1* and *FN1* were significantly up-regulated in TM and TCP groups (Fig. S5), which was consistent with the fact that the overexpression of ECM could facilitate the EMT process [32].

All together, the above findings demonstrated that dAM promoted the growth of iRPE cells by down-regulating expression of ECM promoting genes in iRPE cells, thus inhibiting the ECM process.

3.6. Transplantation of the tissue-engineered iRPE sheets into subretinal space of the rabbits

To further analyze the feasibility of transplantation, we grafted the tissue-engineered dAM-iRPE sheets into rabbits' eyes. 7 days after surgery, multi-color and BAF fundus images identified the grafted sheets with the GFP-positive RPE cells (Fig. 7A-B). OCT imaging revealed that they were located in the subretinal space (Fig. 7C). Immunostaining confirmed that GFP labeled human iRPE cells positive for STEM121 (a human specific marker) survived, kept in monolayer and expressed specific RPE markers including ZO-1, CRALBP and BEST1 in the back of rabbits' eyes (Fig. 7D, E). Cell proliferation was not obviously observed in the iRPE patch (Fig. 7F). Importantly, the grafted RPE cells on dAM was not expressed EMT marker α-SMA (Fig. 7G), being consistent to the anti-EMT effect of dAM *in vitro* described above. These results demonstrated dAM would be a suitable scaffold in the application of iRPE transplantation.

4. Discussion

In this research, we developed a dAM-based scaffold chamber for the generation of iRPE sheets with easy handling and simple fixation. iRPE cells on dAM exhibited morphological features similar to RPE cells *in vivo* with an enhancement of pigmentation and cellular function. Under a comprehensive analysis of transcriptome profiles in iRPE on dAM by RNA-seq, we identified the up-regulation of RPE-specific genes in iRPE on dAM was potentially because dAM inhibited EMT process in iRPE cultivation. dAM-iRPE sheets survived with mature RPE markers expression when transplanted into the subretinal space of rabbits. This authentic dAM-iRPE sheets should facilitate not only the cell replacement therapy for retinal degenerative diseases but also the disease modeling for RPE-related disorders such as AMD.

Although many approaches have been developed to culture RPE cells, the generation of authentic RPE monolayer is still challenging. The healthy structure of native RPE has been described as a monolayer of cobblestone-like hexagonal shape to achieve the key functions such as barrier function and metabolite transport. Aging and the pathogenesis of RPE cause morphometric changes, including the lower density, bigger cell size and smaller ratio of hexagonal shape [27]. Previous studies have shown that the features of cultured RPE cells depend on the culture conditions including the culture medium, substrate or culture vessel [33–36]. TCP is the most common vessel used to expand RPE cells *in vitro*. Differences

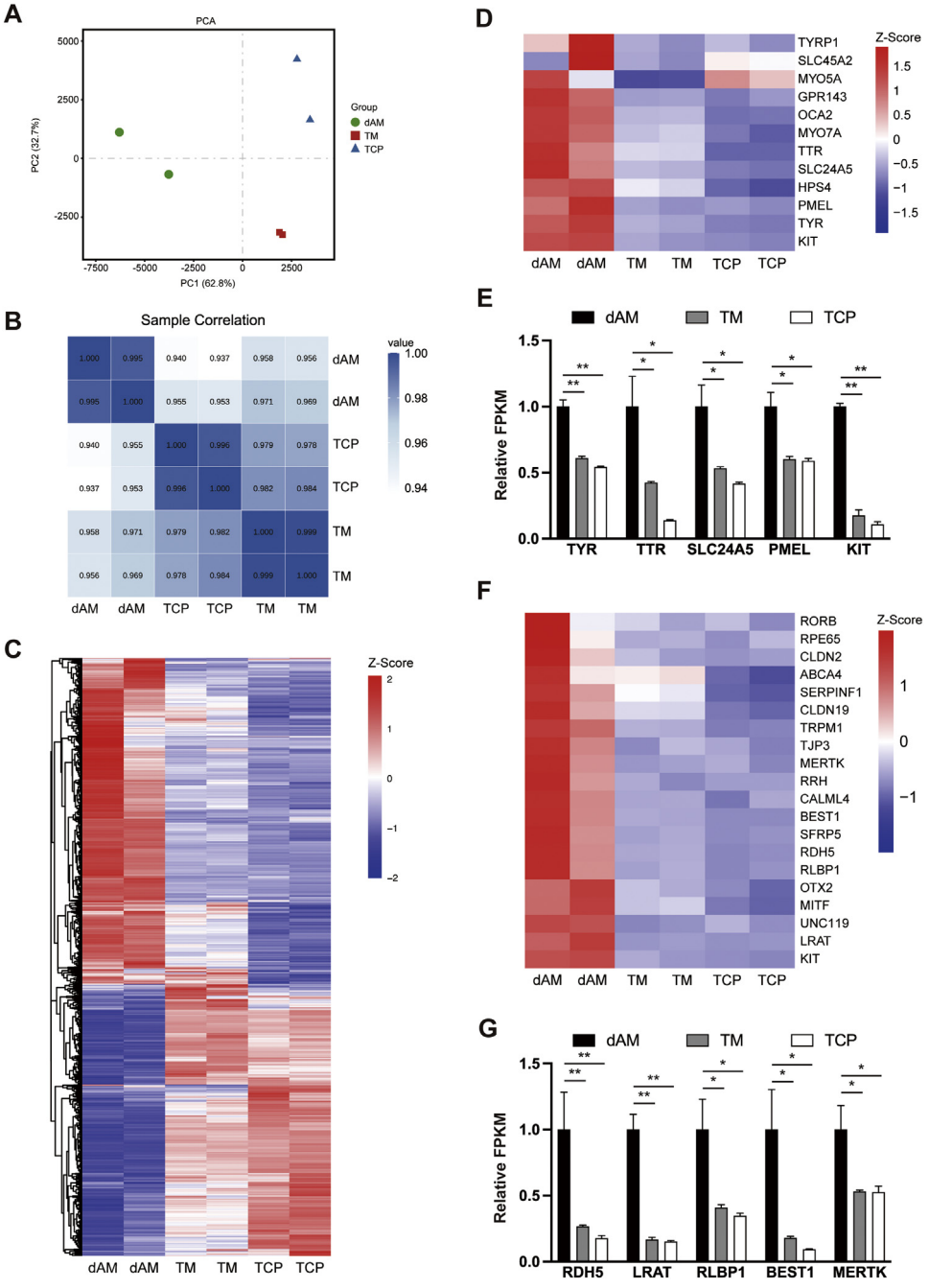

Fig. 5. Verification of RPE maturation and function in iRPE on dAM by RNA-seq analysis. (A) Principal-component analysis of RNA-seq data from iRPE cells on three different substrates. (B) Sample to sample distance between iRPE sheet samples from each group. (C) Heatmap of the DEGs among iRPE on three different substrates. (D) Heatmap of the differential expression of melanin metabolism related genes among iRPE cells on different scaffolds. (E) Relative FPKM value of TYR, TTR, SLC24A5, PMEL and KIT among iRPE cells on three different substrates. Values were expressed as mean ± SD (n = 2). * $P < 0.05$; ** $P < 0.01$, compared to dAM. FPKM, fragments per kilobase per million reads. (F) Heatmap of the differential expression of maturation and functional process related genes among iRPE cells on different scaffolds. (G) Relative FPKM value of RDH5, LRAT, RLBP1, BEST1 and MERTK among iRPE cells on three different substrates. Values were expressed as mean ± SD ($n = 2$). * $P < 0.05$; ** $P < 0.01$, compared to dAM. FPKM, fragments per kilobase per million reads.

in morphology and gene expression have been identified between RPE cultured on TCP and native RPE [37]. Some RPE cells even show the elongated cell shape in multilayers [38]. Transwell contains a semi-permeable insert, which helps epithelial cells to grow into a polarized epithelial monolayer under more natural condition, and is commonly used in the generation and functional evaluation of iRPE sheets [39]. However, compared to native RPE, RPE on transwell presents different features including the thickness, the number of melanosomes and the expression of some RPE signature genes, which may be due to the absence of suitable stiffness and ECM in the membrane of transwell inserts [40]. Natural scaffolds with similar properties to BM, such as dAM, are considered as a promising way to generate authentic RPE monolayer (Table 2). In addition to the similar tensile elastic modulus between BM and dAM, we also used AFM to measure the Young's modulus of the surface of a material in nanoscale, which also proved that the stiff-

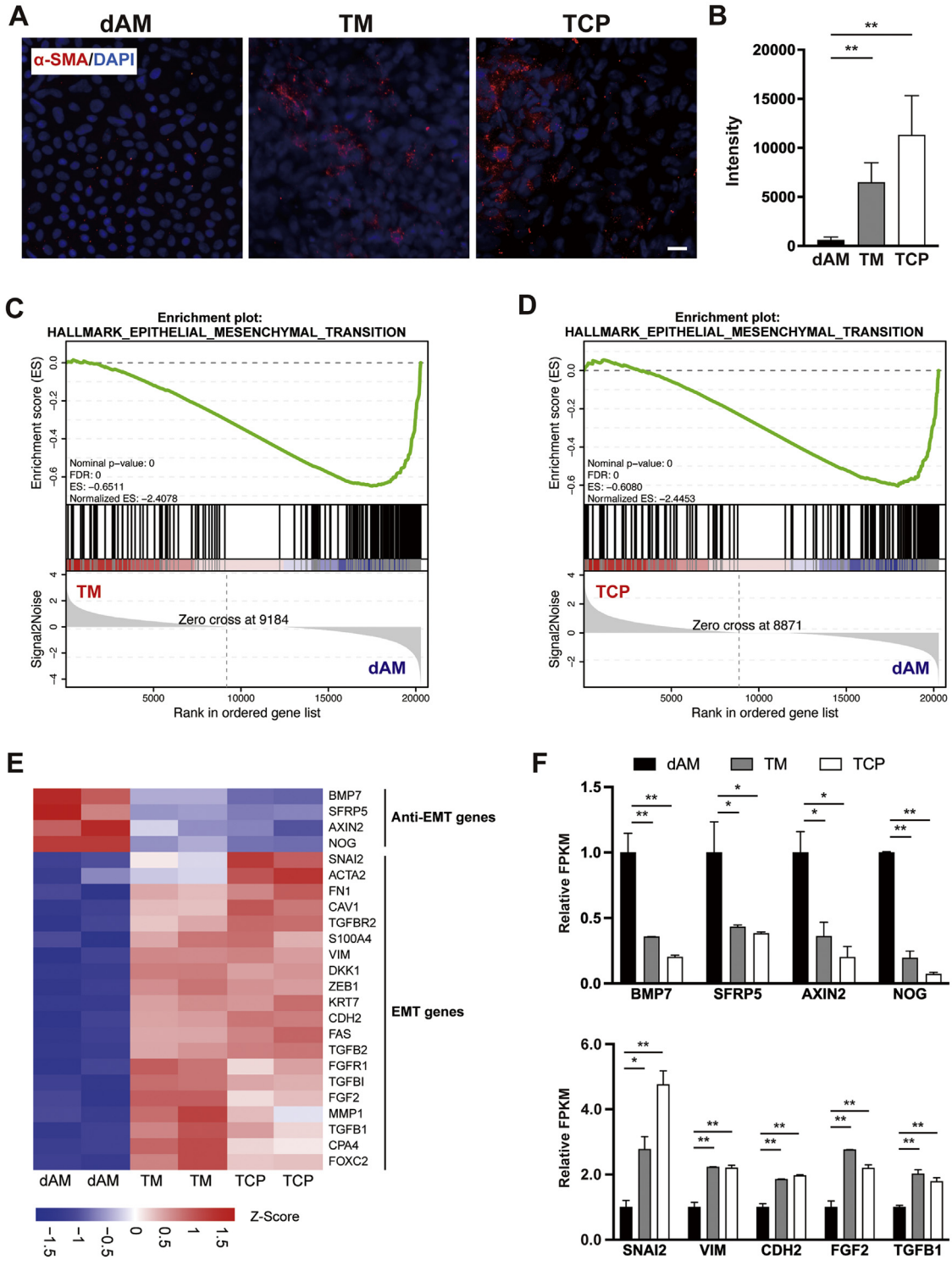

Fig. 6. Identification of the anti-EMT effect of dAM by RNA-seq analysis. (A) Representative immunostaining images for α-SMA in iRPE sheets on different scaffolds. Scale bar = 20 μm. (B) Quantification of the intensity of α-SMA in iRPE cells on different scaffolds. Values were expressed as mean ± SD ($n = 3 \sim 4$). ** $P < 0.01$, compared with dAM. (C, D) Down-regulation of EMT genes in iRPE on dAM compared with TM (C) or TCP (D) by Gene set enrichment analysis (GSEA). Normalized enrichment score (ES) and normalized P values were shown. (E) Heatmap of the differential expression of EMT-related genes and anti-EMT genes among iRPE on three different substrates. EMT-related genes were down-regulated and anti-EMT genes were up-regulated in iRPE on dAM. (F) Relative FPKM value of anti-EMT genes (BMP7, SFRP5, AXIN2, NOG) and EMT genes (SNAI2, VIM, CDH2, FGF2, TGFB1) among iRPE cells on three different substrates. Values were expressed as mean ± SD ($n = 2$). * $P < 0.05$; ** $P < 0.01$, compared to dAM.

Table 2
Components and elasticity of Bruch's membrane and amniotic membrane.

Component	Bruch's membrane	Amniotic membrane	References
Collagens	I, III, IV, V, VI, XIII	I, III, IV, V, VI, VII, XVI, XVII	[11,60]
Laminin	√	√	[11,60]
Nidogen	√	√	[11,60]
Fibronectin	√	√	[11,60]
Heparan sulphate	√	√	[11,60]
Chondroitin/ Dermatan sulphate	√	√	[11,60]
Elastin	√	√	[11,60]
Pentraxin	√	√	[11,60]
Young's modulus (Tension)	1.0–5.0 MPa	2.8 MPa	[61,62]

ness of the surface of dAM was similar to the retina [41]. Several researches attempted to culture RPE cells on dAM which was fastened to transwells or glass slides, showing dAM-based RPE cells had typical morphological and molecular features [38,42]. In this research, we used the Minucells tissue carriers to simply fix dAM and established a cost-effective dAM scaffold chamber for iRPE cells culture and transplantation. RPE cells increased pigmentation and expression of RPE-specific markers on dAM, which was consistent with previous reports [38,42]. In addition, RNA-seq analysis disclosed the transcriptome changes in iRPE cells on dAM. Compared to iRPE cells on TCP or TM, a more significant difference was identified in iRPE cells on dAM with up-regulation of a broad range of melanin metabolism genes such as TYR, TTR, PMEL and RPE functional genes such as RDH5, LRAT, RLBP1, BEST1 and MERTK. The detailed analysis from morphological and functional features to transcriptome profiles indicated that our tissue-engineered iRPE sheets were authentic.

EMT of RPE cells is a key pathological event in severe retinal diseases such as proliferative vitreoretinopathy and diabetic retinopathy [43–45], which is the common event occurred in the cultivation of RPE cells and the potential cause of the failure of RPE grafts in cell therapies [13]. Many efforts have been made to intervene in this transition of RPE cells *in vitro* and *in vivo*, such as by the addition of ROCK-inhibitor [46] or TGF-β signaling inhibitor [47]. When cultured iRPE cells on dAM, the de-differentiated cells were seldom identified. The cellular responses of iRPE cells on different scaffolds were analyzed by phalloidin staining. iRPE on dAM exhibited the circumferential actin belt, whereas cells on TM and TCP exhibited more stress fiber. We further found that dAM had the lowest values of the Young's modulus among three scaffolds by AFM measurement. According to the previous report that stress fiber was an important feature of the onset of EMT [48], our results indicated that the mechanical property was a key factor of dAM to prevent EMT. In addition, transcriptome analysis showed that dAM inhibited the expression of EMT markers, such as SNAI2, VIM, CDH2, FGF2 and TGFB1, but induced the expression of anti-EMT markers, such as BMP7, SFRP5, AXIN2 and NOG. Moreover, when transplanted into the subretinal space of rabbits, dAM-iRPE sheets did not undergo EMT, which was considered as a risk following RPE transplantation [9,49]. These findings imply that the dAM-based RPE sheets were suitable for retinal reconstruction.

Furthermore, preclinical and clinical studies on RPE cell transplantation indicate that inflammation also contributes to the rejection of the transplanted RPE cells although RPE is considered as an immune-privileged tissue [50–52]. Some reports have revealed that RPE cells have immunogenic properties including the secretion of inflammatory cytokines and chemokines [53]. Therefore, reducing the expression of inflammatory cytokines and suppressing the recruitment of immune cells are also needed to consider during scaffold design. The clinical applications of hAM have shown its immune-privileged property by suppressing the alloreactive T cells [54]. In the current study, we also explored the impact of dAM on inflammatory cytokines of RPE cells. iRPE cells in the dAM group down-regulated the expression of inflammatory cytokines including CXCL6, IL11 and CCL20, compared to the TM and TCP group (Fig. S5), which suggested that dAM could prevent the inflammatory response in iRPE transplantation. These results revealed the possibility that dAM-iRPE sheets would be a more suitable material source for transplantation. Further experiments with these dAM-iRPE sheets need to be carried out to evaluate the therapeutic effects in animal models with retinal degenerations. iRPE cells from patient-derived hiPSCs have the potential to model the pathogenesis of inherited retinal diseases. RP and AMD patients-derived iRPEs have already been used to analyze the disease initiation and progression [2,55]. Pathological analysis of AMD suggests that drusen formation with the accumulation of oxidized molecules and neutral fats in BM may be the initiating event that causes macular dysfunction [11]. Therefore, acquiring a BM-RPE co-culture model is the prerequisite to faithfully recapitulate the pathogenesis of these diseases. Previous studies along our current findings indicate that cultured iRPEs on tissue culture plate or transwell may not be a good model for this purpose due to the absence of BM and natural mechanical properties. In contrast, hAM had similar components to BM including the ECM components and stiffness, and iRPE cells on dAM presented authentic features of primary RPE *in vivo*, hence, dAM-iRPE sheets may be a better model to understand the onset and progress of retinal diseases. To our knowledge, little attempt has been made to model pathogenesis using the co-culture of patient iRPE and dAM [56].

To achieve the stable and reproducible generation of dAM-iRPE sheets, a key step is to find a suitable material to hold or fix the soft dAM in its right orientation and tension. Although some other researchers have tried to fix or fasten dAM on inserts for cell culture [21,57], the interference of other materials would make dAM hard to keep the appropriate tension. Tissue carriers have been used in modeling an *ex-vivo* retina-RPE tissue [58]. In this study, we used the Minucells tissue carriers to simply clip dAM without other support to construct the dAM chamber with high reproducibility (see details in Materials and Methods section 2.2). The dAM chambers can be placed in 24-,12- or 6-well culture plates, facilitating cell culture. In addition, the tissue carriers can be reused after sterilization, reducing experiment expenses. This cost-effective dAM chamber would be an ideal system for dAM-based cell cultures, which should contribute to cell therapy and disease modeling using iRPE cells. Nevertheless, this device cannot isolate the culture vessel into two compartments, which is necessary for analyzing the polarized secretion of cytokine and evaluating the barrier function by transepithelial resistance [59]. Although the higher amount of VEGF secretion and immunostaining for integrin-β1 indicated that iRPE cells on dAM had a better polarization and barrier function, further adjustment would be necessary to establish a chamber with the separation of the apical side and basal side like transwell.

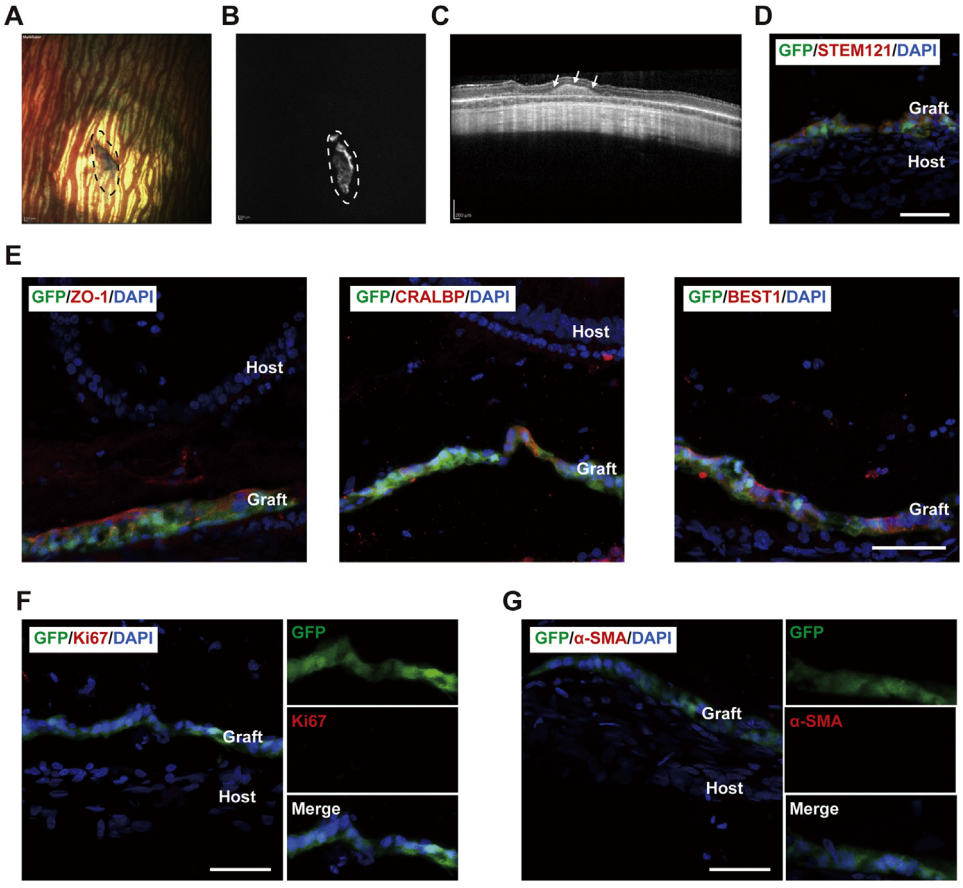

Fig. 7. Transplantation of dAM-iRPE sheets into subretinal space of rabbit. (A, B, C) Multi-color fundus photograph, BAF photograph and SD-OCT images of a rabbit with iRPE sheets transplantation for 7 days. Scale bar = 200 μm. Dashed line circle indicated the GFP positive area (A, B). Arrows indicated the location of iRPE patch (C). (D-G) Representative immunostaining images of rabbit's retina 7 days after transplantation. D, STEM121 (a human specific marker). E, ZO-1, CRALBP and BEST1 (RPE-specific markers). F, Ki67 (a cell proliferation marker). G, α-SMA (a EMT marker). Scale bar = 50 μm.

5. Conclusion

In this research, we have shown that the engineered iRPE sheets on decellularized hAM contribute to enhancing both the morphological and functional features. Transcriptomic analysis of iRPE sheets demonstrates the superiority of the dAM-based cultures, including the activation of RPE functional markers and the suppression of EMT-related markers and inflammatory cytokines when compared to iRPE sheets on transwells or culture plates. Furthermore, when grafted into rabbits' eyes, dAM-iRPE sheets survive and keep monolayer without EMT. Therefore, our engineered dAM-iRPE sheets have the potential to be used in the field of regenerative therapy, disease modeling and drug screening for retinal disorders such as AMD and RP.

Declaration of Competing Interest

The authors declare that they have no known competing financial interests or personal relationships that could have appeared to influence the work reported in this paper.

Acknowledgments

We thank Dr. Li Gong for technical support in Young's modulus measurement by AFM. We would like to acknowledge the Eye Bank of Guangdong Province, China for their supply of hAM biomaterial. This work was supported partly from the National Natural Science Foundation of China (81970842 and 82172957); Science & Technology Project of Guangdong Province (2017B020230003); National Key Research and Development Program of the Ministry of Science and Technology (2017YFA0104101); a Joint grant from Science & Technology Project of Guangzhou and Zhongshan Ophthalmic Center, Sun Yat-sen University (202201020312) and the Fundamental Research Funds of the State Key Laboratory of Ophthalmology.

Supplementary materials

Supplementary materials associated with this article can be found, in the online version, at doi:10.1016/j.actbio.2022.07.064.

References

[1] O. Strauss, The retinal pigment epithelium in visual function, Physiol. Rev. 85 (2005) 845–881, doi:10.1152/physrev.00021.2004.
[2] C.A. Galloway, S. Dalvi, S.S.C. Hung, L.A. MacDonald, L.R. Latchney, R.C.B. Wong, R.H. Guymer, D.A. Mackey, D.S. Williams, M.M. Chung, D.M. Gamm, A. Pébay, A.W. Hewitt, R. Singh, Drusen in patient-derived hiPSC-RPE models of macular dystrophies, Proc. Natl. Acad. Sci. USA 114 (2017) E8214–E8223, doi:10.1073/pnas.1710430114.
[3] K.V. Manian, C.A. Galloway, S. Dalvi, A.A. Emanuel, J.A. Mereness, W. Black, L. Winschel, C. Soto, Y. Li, Y. Song, W. DeMaria, A. Kumar, I. Slukvin, M.P. Schwartz, W.L. Murphy, B. Anand-Apte, M. Chung, D.S.W. Benoit, R. Singh, 3D iPSC modeling of the retinal pigment epithelium-choriocapillaris complex identifies factors involved in the pathology of macular degeneration, Cell Stem Cell 28 (2021) 846–862.e8, doi:10.1016/j.stem.2021.02.006.
[4] S.D. Schwartz, J.-P. Hubschman, G. Heilwell, V. Franco-Cardenas, C.K. Pan, R.M. Ostrick, E. Mickunas, R. Gay, I. Klimanskaya, R. Lanza, Embryonic stem cell trials for macular degeneration: a preliminary report, Lancet 379 (2012) 713–720, doi:10.1016/S0140-6736(12)60028-2.
[5] W.K. Song, K.M. Park, H.J. Kim, J.H. Lee, J. Choi, S.Y. Chong, S.H. Shim, L.V. Del Priore, R. Lanza, Treatment of macular degeneration using embryonic stem cell-derived retinal pigment epithelium: preliminary results in Asian patients, Stem Cell Rep. 4 (2015) 860–872, doi:10.1016/j.stemcr.2015.04.005.

[6] M. Mandai, A. Watanabe, Y. Kurimoto, Y. Hirami, C. Morinaga, T. Daimon, M. Fujihara, H. Akimaru, N. Sakai, Y. Shibata, M. Terada, Y. Nomiya, S. Tanishima, M. Nakamura, H. Kamao, S. Sugita, A. Onishi, T. Ito, K. Fujita, S. Kawamata, M.J. Go, C. Shinohara, K. Hata, M. Sawada, M. Yamamoto, S. Ohta, Y. Ohara, K. Yoshida, J. Kuwahara, Y. Kitano, N. Amano, M. Umekage, F. Kitaoka, A. Tanaka, C. Okada, N. Takasu, S. Ogawa, S. Yamanaka, M. Takahashi, Autologous induced stem-cell–derived retinal cells for macular degeneration, N. Engl. J. Med. 376 (2017) 1038–1046, doi:10.1056/NEJMoa1608368.

[7] M.S. Mehat, V. Sundaram, C. Ripamonti, A.G. Robson, A.J. Smith, S. Borooah, M. Robinson, A.N. Rosenthal, W. Innes, R.G. Weleber, R.W.J. Lee, M. Crossland, G.S. Rubin, B. Dhillon, D.H.W. Steel, E. Anglade, R.P. Lanza, R.R. Ali, M. Michaelides, J.W.B. Bainbridge, Transplantation of human embryonic stem cell-derived retinal pigment epithelial cells in macular degeneration, Ophthalmology 125 (2018) 1765–1775, doi:10.1016/J.OPHTHA.2018.04.037.

[8] Y. Liu, H.W. Xu, L. Wang, S.Y. Li, C.J. Zhao, J. Hao, Q.Y. Li, T.T. Zhao, W. Wu, Y. Wang, Q. Zhou, C. Qian, L. Wang, Z.Q. Yin, Human embryonic stem cell-derived retinal pigment epithelium transplants as a potential treatment for wet age-related macular degeneration, Cell Discov. 4 (2018) 50, doi:10.1038/s41421-018-0053-y.

[9] L. da Cruz, K. Fynes, O. Georgiadis, J. Kerby, Y.H. Luo, A. Ahmado, A. Vernon, J.T. Daniels, B. Nommiste, S.M. Hasan, S.B. Gooljar, A.-J.F. Carr, A. Vugler, C.M. Ramsden, M. Bictash, M. Fenster, J. Steer, T. Harbinson, A. Wilbrey, A. Tufail, G. Feng, M. Whitlock, A.G. Robson, G.E. Holder, M.S. Sagoo, P.T. Loudon, P. Whiting, P.J. Coffey, Phase 1 clinical study of an embryonic stem cell–derived retinal pigment epithelium patch in age-related macular degeneration, Nat. Biotechnol. 36 (2018) 328–337, doi:10.1038/nbt.4114.

[10] B. Diniz, P. Thomas, B. Thomas, R. Ribeiro, Y. Hu, R. Brant, A. Ahuja, D. Zhu, L. Liu, M. Koss, M. Maia, G. Chader, D.R. Hinton, M.S. Humayun, Subretinal Implantation of retinal pigment epithelial cells derived from human embryonic stem cells: improved survival when implanted as a monolayer, Invest. Ophthalmol. Vis. Sci. 54 (2013) 5087–5096, doi:10.1167/iovs.12-11239.

[11] J.C. Booij, D.C. Baas, J. Beisekeeva, T.G.M.F. Gorgels, A.A.B. Bergen, The dynamic nature of Bruch's membrane, Prog. Retin. Eye Res. 29 (2010) 1–18, doi:10.1016/j.preteyeres.2009.08.003.

[12] S. Beatty, H.H. Koh, M. Phil, D. Henson, M. Boulton, The role of oxidative stress in the pathogenesis of age-related macular degeneration, Surv. Ophthalmol. 45 (2000) 115–134, doi:10.1016/S0039-6257(00)00140-5.

[13] R. Sharma, V. Khristov, A. Rising, B.S. Jha, R. Dejene, N. Hotaling, Y. Li, J. Stoddard, C. Stankewicz, Q. Wan, C. Zhang, M.M. Campos, K.J. Miyagishima, D. McGaughey, R. Villasmil, M. Mattapallil, B. Stanzel, H. Qian, W. Wong, L. Chase, S. Charles, T. McGill, S. Miller, A. Maminishkis, J. Amaral, K. Bharti, Clinical-grade stem cell-derived retinal pigment epithelium patch rescues retinal degeneration in rodents and pigs, Sci. Transl. Med. 11 (2019) eaat5580, doi:10.1126/scitranslmed.aat5580.

[14] K.J. McHugh, S.L. Tao, M. Saint-Geniez, Porous poly(ε-caprolactone) scaffolds for retinal pigment epithelium transplantation, Investig. Ophthalmol. Vis. Sci. 55 (2014) 1754–1762, doi:10.1167/iovs.13-12833.

[15] P.H. Warnke, M. Alamein, S. Skabo, S. Stephens, R. Bourke, P. Heiner, Q. Liu, Primordium of an artificial Bruch's membrane made of nanofibers for engineering of retinal pigment epithelium cell monolayers, Acta Biomater. 9 (2013) 9414–9422, doi:10.1016/j.actbio.2013.07.029.

[16] A.T. Christiansen, S.L. Tao, M. Smith, G.E. Wnek, J.U. Prause, M.J. Young, H. Klassen, H.J. Kaplan, M.La Cour, J.F. Kiilgaard, Subretinal implantation of electrospun, short nanowire, and smooth poly(ε-caprolactone) scaffolds to the subretinal space of porcine eyes, Stem Cells Int. (2012) 2012, doi:10.1155/2012/454295.

[17] G. Thumann, U. Schraermeyer, K.U. Bartz-Schmidt, K. Heimann, Descemet's membrane as membranous support in RPE/IPE transplantation, Curr. Eye Res. 16 (1997) 1236–1238, doi:10.1076/ceyr.16.12.1236.5031.

[18] U. Hartmann, F. Sistani, U.H. Steinhorst, Human and porcine anterior lens capsule as support for growing and grafting retinal pigment epithelium and iris pigment epithelium, Graefe's Arch, Clin. Exp. Ophthalmol. 237 (1999) 940–945, doi:10.1007/s004170050390.

[19] A.C. Mamede, M.J. Carvalho, A.M. Abrantes, M. Laranjo, C.J. Maia, M.F. Botelho, Amniotic membrane: from structure and functions to clinical applications, Cell Tissue Res. 349 (2012) 447–458, doi:10.1007/s00441-012-1424-6.

[20] C. Capeéans, A. Piñeiro Ces, M. Pardo, C. Sueiro-López, M.J. Blanco, F. Domínguez, M. Sánchez-Salorio, Amniotic membrane as support for human retinal pigment epithelium (RPE) cell growth, Acta Ophthalmol. Scand. 81 (2003) 271–277, doi:10.1034/j.1600-0420.2003.00076.x.

[21] K. Ben M'Barek, W. Habeler, A. Plancheron, M. Jarraya, F. Regent, A. Terray, Y. Yang, L. Chatrousse, S. Domingues, Y. Masson, J.-A. Sahel, M. Peschanski, O. Goureau, C. Monville, Human ESC-derived retinal epithelial cell sheets potentiate rescue of photoreceptor cell loss in rats with retinal degeneration, Sci. Transl. Med. 9 (2017), doi:10.1126/scitranslmed.aai7471.

[22] P. Trosan, I. Smeringaiova, K. Brejchova, J. Bednar, O. Benada, O. Kofronova, K. Jirsova, The enzymatic de-epithelialization technique determines denuded amniotic membrane integrity and viability of harvested epithelial cells, PLoS One 13 (2018) 1–16, doi:10.1371/journal.pone.0194820.

[23] L. Zhang, D. Zou, S. Li, J. Wang, Y. Qu, S. Ou, C. Jia, J. Li, H. He, T. Liu, J. Yang, Y. Chen, Z. Liu, W. Li, An ultra-thin amniotic membrane as carrier in corneal epithelium tissue-engineering, Sci. Rep. 6 (2016) 1–12, doi:10.1038/srep21021.

[24] S. Liu, B. Xie, X. Song, D. Zheng, L. He, G. Li, G. Gao, F. Peng, M. Yu, J. Ge, X. Zhong, Self-formation of RPE spheroids facilitates enrichment and expansion of hiPSC-derived RPE generated on retinal organoid induction platform, Invest. Ophthalmol. Vis. Sci. 59 (2018) 5659–5669, doi:10.1167/iovs.17-23613.

[25] X. Zhong, C. Gutierrez, T. Xue, C. Hampton, M.N. Vergara, L.H. Cao, A. Peters, T.S. Park, E.T. Zambidis, J.S. Meyer, D.M. Gamm, K.W. Yau, M.V. Canto-Soler, Generation of three-dimensional retinal tissue with functional photoreceptors from human iPSCs, Nat. Commun. 5 (2014), doi:10.1038/ncomms5047.

[26] G. Gao, L. He, S. Liu, D. Zheng, X. Song, W. Zhang, M. Yu, G. Luo, X. Zhong, Establishment of a rapid lesion-controllable retinal degeneration monkey model for preclinical stem cell therapy, Cells 9 (2020) 1–14, doi:10.3390/cells9112468.

[27] S.K. Bhatia, A. Rashid, M.A. Chrenek, Q. Zhang, B.B. Bruce, M. Klein, J.H. Boatright, Y. Jiang, H.E. Grossniklaus, J.M. Nickerson, Analysis of RPE morphometry in human eyes, Mol. Vis. 22 (2016) 898–916 http://www.ncbi.nlm.nih.gov/pubmed/27555739.

[28] N. Parrish, F. Hormozdiari, E. Eskin, Assembly of non-unique insertion content using next-generation sequencing, Bioinf. Impact Accurate Quantif. Proteom. Genet. Anal. Res. (2014) 21–40, doi:10.1201/b16589.

[29] A. Subramanian, P. Tamayo, V.K. Mootha, S. Mukherjee, B.L. Ebert, M.A. Gillette, A. Paulovich, S.L. Pomeroy, T.R. Golub, E.S. Lander, J.P. Mesirov, Gene set enrichment analysis: a knowledge-based approach for interpreting genome-wide expression profiles, Proc. Natl. Acad. Sci. USA 102 (2005) 15545–15550, doi:10.1073/pnas.0506580102.

[30] M. Aragona, T. Panciera, A. Manfrin, S. Giulitti, F. Michielin, N. Elvassore, S. Dupont, S. Piccolo, A mechanical checkpoint controls multicellular growth through YAP/TAZ regulation by actin-processing factors, Cell 154 (2013) 1047–1059, doi:10.1016/j.cell.2013.07.042.

[31] N.C. Boles, M. Fernandes, T. Swigut, R. Srinivasan, L. Schiff, A. Rada-Iglesias, Q. Wang, J.S. Saini, T. Kiehl, J.H. Stern, J. Wysocka, T.A. Blenkinsop, S. Temple, Epigenomic and transcriptomic changes during human RPE EMT in a stem cell model of epiretinal membrane pathogenesis and prevention by nicotinamide, Stem Cell Rep. 14 (2020) 631–647, doi:10.1016/j.stemcr.2020.03.009.

[32] G. Tzanakakis, R.M. Kavasi, K. Voudouri, A. Berdiaki, I. Spyridaki, A. Tsatsakis, D. Nikitovic, Role of the extracellular matrix in cancer-associated epithelial to mesenchymal transition phenomenon, Dev. Dyn. 247 (2018) 368–381, doi:10.1002/dvdy.24557.

[33] D.M. Gamm, J.N. Melvan, R.L. Shearer, I. Pinilla, G. Sabat, C.N. Svendsen, L.S. Wright, A novel serum-free method for culturing human prenatal retinal pigment epithelial cells, Invest. Ophthalmol. Vis. Sci. 49 (2008) 788–799, doi:10.1167/iovs.07-0777.

[34] J. Hu, D. Bok, A cell culture medium that supports the differentiation of human retinal pigment epithelium into functionally polarized monolayers, Mol. Vis. 7 (2001) 14–19.

[35] A. Plaza Reyes, S. Petrus-Reurer, L. Antonsson, S. Stenfelt, H. Bartuma, S. Panula, T. Mader, I. Douagi, H. André, O. Hovatta, F. Lanner, A. Kvanta, Xeno-free and defined human embryonic stem cell-derived retinal pigment epithelial cells functionally integrate in a large-eyed preclinical model, Stem Cell Rep. 6 (2016) 9–17, doi:10.1016/j.stemcr.2015.11.008.

[36] H. Tian, J.Y. Xu, Y. Tian, Y. Cao, C. Lian, Q. Ou, B. Wu, C. Jin, F. Gao, J. Wang, J. Zhang, J. Zhang, W. Li, L. Lu, G.T. Xu, A cell culture condition that induces the mesenchymal-epithelial transition of dedifferentiated porcine retinal pigment epithelial cells, Exp. Eye Res. 177 (2018) 160–172, doi:10.1016/j.exer.2018.08.005.

[37] J. Tian, K. Ishibashi, S. Honda, S.A. Boylan, L.M. Hjelmeland, J.T. Handa, The expression of native and cultured human retinal pigment epithelial cells grown in different culture conditions, Br. J. Ophthalmol. 89 (2005) 1510–1517, doi:10.1136/bjo.2005.072108.

[38] K. Ohno-Matsui, S. Ichinose, K.I. Nakahama, T. Yoshida, A. Kojima, M. Mochizuki, I. Morita, The effects of amniotic membrane on retinal pigment epithelial cell differentiation, Mol. Vis. 11 (2005) 1–10.

[39] S. Sonoda, C. Spee, E. Barron, S.J. Ryan, R. Kannan, D.R. Hinton, A protocol for the culture and differentiation of highly polarized human retinal pigment epithelial cells, Nat. Protoc. 4 (2009) 662–673, doi:10.1038/nprot.2009.33.

[40] Y. Miura, Retinal pigment epithelium-choroid organ culture, Expert Rev. Ophthalmol. 6 (2011) 669–680, doi:10.1586/eop.11.70.

[41] K. Franze, M. Francke, K. Günter, A.F. Christ, N. Kö rber, A. Reichenbach, J. Guck, Spatial mapping of the mechanical properties of the living retina using scanning force microscopy, Soft Matter 7 (2011) 3147–3154, doi:10.1039/c0sm01017k.

[42] H. Akrami, Z.S. Soheili, M. Sadeghizadeh, K. Khalooghi, H. Ahmadieh, M.R. Kanavi, S. Samiei, J. Pakravesh, Evaluation of RPE65, CRALBP, VEGF, CD68, and Tyrosinase gene expression in human retinal pigment epithelial cells cultured on amniotic membrane, Biochem. Genet. 49 (2011) 313–322, doi:10.1007/s10528-010-9409-1.

[43] S. Saika, O. Yamanaka, Y. Okada, S.I. Tanaka, T. Miyamoto, T. Sumioka, A. Kitano, K. Shirai, K. Ikeda, TGFβ in fibroproliferative diseases in the eye, Front. Biosci. (Schol Ed) 1 (2009) 376–390, doi:10.2741/S32.

[44] S. Tamiya, H.J. Kaplan, Role of epithelial-mesenchymal transition in proliferative vitreoretinopathy, Exp. Eye Res. 142 (2016) 26–31, doi:10.1016/j.exer.2015.02.008.

[45] J.A. Jerdan, J.S. Pepose, R.G. Michels, H. Hayashi, S. De Bustros, M. Sebag, B.M. Glaser, Proliferative vitreoretinopathy membranes: an immunohistochemical study, Ophthalmology 96 (1989) 801–810, doi:10.1016/S0161-6420(89)32818-1.

[46] R.H. Croze, D.E. Buchholz, M.J. Radeke, W.J. Thi, Q. Hu, P.J. Coffey, D.O. Clegg, ROCK inhibition extends passage of pluripotent stem cell-derived retinal pigmented epithelium, Stem Cells Transl. Med. 3 (2014) 1066–1078, doi:10.5966/sctm.2014-0079.

[47] Y. Chen, B. Wu, J.F. He, J. Chen, Z.W. Kang, D. Liu, J. Luo, K. Fang, X. Leng, H. Tian, J. Xu, C. Jin, J. Zhang, J. Wang, J. Zhang, Q. Ou, L. Lu, F. Gao, G.T. Xu, Ef-

fectively intervening epithelial-mesenchymal transition of retinal pigment epithelial cells with a combination of ROCK and TGF-β signaling inhibitors, Investig. Ophthalmol. Vis. Sci. 62 (2021) 1–14, doi:10.1167/iovs.62.4.21.
[48] W. Zhang, H. Han, Targeting matrix stiffness-induced activation of retinal pigment epithelial cells through the RhoA/YAP pathway ameliorates proliferative vitreoretinopathy, Exp. Eye Res. 209 (2021) 108677, doi:10.1016/j.exer.2021.108677.
[49] D.G. Charteris, Proliferative vitreoretinopathy: pathobiology, surgical management, and adjunctive treatment, Br. J. Ophthalmol. 79 (1995) 953–960, doi:10.1136/bjo.79.10.953.
[50] D. Keegan, K.P. Kennelly, T.M. Holmes, D.M. Wallace, D.J. Keegan, Early subretinal allograft rejection is characterized by innate immune activity, Cell Transplant 26 (2017) 983–1000, doi:10.3727/096368917X694697.
[51] T.J. McGill, J. Stoddard, A.M. Renner, I. Messaoudi, K. Bharti, S. Mitalipov, A. Lauer, D.J. Wilson, M. Neuringer, Allogeneic iPSC-derived RPE cell graft failure following transplantation into the subretinal space in nonhuman primates, Investig. Ophthalmol. Vis. Sci. 59 (2018) 1374–1383, doi:10.1167/iovs.17-22467.
[52] E.H. Sohn, C. Jiao, E. Kaalberg, C. Cranston, R.F. Mullins, E.M. Stone, B.A. Tucker, Allogenic iPSC-derived RPE cell transplants induce immune response in pigs: a pilot study, Sci. Rep. 5 (2015) 1–10, doi:10.1038/srep11791.
[53] S. Sugita, M. Mandai, H. Kamao, M. Takahashi, Immunological aspects of RPE cell transplantation, Prog. Retin. Eye Res. 84 (2021) 100950, doi:10.1016/j.preteyeres.2021.100950.
[54] M. Ueta, M.N. Kweon, Y. Sano, C. Sotozono, J. Yamada, N. Koizumi, H. Kiyono, S. Kinoshita, Immunosuppressive properties of human amniotic membrane for mixed lymphocyte reaction, Clin. Exp. Immunol. 129 (2002) 464–470, doi:10.1046/j.1365-2249.2002.01945.x.
[55] A. Milenkovic, C. Brandl, V.M. Milenkovic, T. Jendryke, L. Sirianant, P. Wanitchakool, S. Zimmermann, C.M. Reiff, F. Horling, H. Schrewe, R. Schreiber, K. Kunzelmann, C.H. Wetzel, B.H.F. Weber, Bestrophin 1 is indispensable for volume regulation in human retinal pigment epithelium cells, Proc. Natl. Acad. Sci. USA 112 (2015) E2630–E2639, doi:10.1073/pnas.1418840112.
[56] L. Krishna, K. Dhamodaran, M. Subramani, M. Ponnulagu, N. Jeyabalan, S.R. Krishna Meka, C. Jayadev, R. Shetty, K. Chatterjee, S.S. Khora, D. Das, Protective role of decellularized human amniotic membrane from oxidative stress-induced damage on retinal pigment epithelial cells, ACS Biomater. Sci. Eng. 5 (2019), doi:10.1021/acsbiomaterials.8b00769.
[57] D. Meller, S.C.G. Tseng, Conjunctival epithelial cell differentiation on amniotic membrane, Investig. Ophthalmol. Vis. Sci. 40 (1999) 878–886.
[58] K. Kobuch, W.A. Herrmann, C. Framme, H.G. Sachs, V.P. Gabel, J. Hillenkamp, Maintenance of adult porcine retina and retinal pigment epithelium in perfusion culture: characterisation of an organotypic in vitro model, Exp. Eye Res. 86 (2008) 661–668, doi:10.1016/j.exer.2008.01.011.
[59] K. Ye, Y. Takemoto, A. Ito, M. Onda, N. Morimoto, M. Mandai, M. Takahashi, R. Kato, F. Osakada, Reproducible production and image-based quality evaluation of retinal pigment epithelium sheets from human induced pluripotent stem cells, Sci. Rep. 10 (2020) 14387, doi:10.1038/s41598-020-70979-y.
[60] H. Niknejad, H. Peirovi, M. Jorjani, A. Ahmadiani, J. Ghanavi, A.M. Seifalian, Properties of the amniotic membrane for potential use in tissue engineering, Eur. Cells Mater. 15 (2008) 88–99, doi:10.22203/ecm.v015a07.
[61] J. Benson-Martin, P. Zammaretti, G. Bilic, T. Schweizer, B. Portmann-Lanz, T. Burkhardt, R. Zimmermann, N. Ochsenbein-Kölble, The Young's modulus of fetal preterm and term amniotic membranes, Eur. J. Obstet. Gynecol. Reprod. Biol. 128 (2006) 103–107, doi:10.1016/j.ejogrb.2005.12.011.
[62] R.F. Fisher, The influence of age on some ocular basement membranes, Eye 1 (1987) 184–189, doi:10.1038/eye.1987.35.